

Mechanistic Insights into Potassium-Assistant Thermal-Catalytic Oxidation of Soot over Single-Crystalline SrTiO_3 Nanotubes with Ordered Mesopores

Fan Fang,* Fang Xu, Xue Li, Chong Chen, Nengjie Feng,* Yijiao Jiang, and Jun Huang*



Cite This: ACS Catal. 2025, 15, 789–799



Read Online

ACCESS |

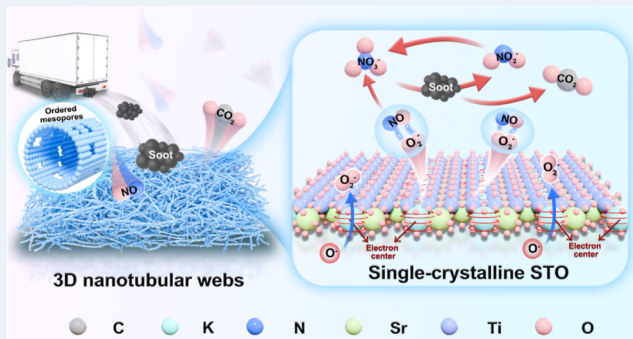
Metrics & More

Article Recommendations

Supporting Information

ABSTRACT: Soot catalytic combustion using single-crystalline perovskite-type materials holds great promise as an efficient non-noble metal catalyst, with K^+ -modified SrTiO_3 emerging as one of the most desirable candidates. However, balancing the crystallinity and an optimized pore structure and revealing the mechanism underlying the K^+ action remain challenges. Herein, by the electrospinning technique, we successfully self-assembled the K-doped single-crystalline $\text{SrTi}_{0.95}\text{Al}_{0.05}\text{O}_3$ nanotubular webs with ordered mesopores. The good crystallinity and mesoporous structures contribute to the enhanced catalytic performance with desirable stability. Based on comprehensive characterizations and density functional theory (DFT) calculations, K^+ ions effectively accumulate defect charges, facilitating the generation of additional oxygen vacancies and expediting oxygen activation during the reaction. Additionally, the presence of K^+ ions prefers to preserve O_2 bond integrity during activation, significantly increasing NO adsorption capacity. Utilizing KNO_3 as the medium, K^+ effectively facilitates the storage and subsequent release of active oxygen species, leading to the promised catalytic performance ($T_{50} = 368^\circ\text{C}$, $E_a = 64.97 \text{ kJ mol}^{-1}$, $\text{TOF}_\text{K} = 0.017 \text{ h}^{-1}$). This study provides mechanistic insights into developing advanced materials for thermal catalytic heterogeneous reactions.

KEYWORDS: soot catalytic combustion, single-crystalline perovskites, nanotubular webs, ordered mesopores, K^+ ions, DFT calculations



1. INTRODUCTION

Motor vehicles and vessels play crucial roles in facilitating economic production activities, emitting soot particles as the significant constituent of fine particulate matter (PM2.5).^{1,2} Particularly, they can adsorb many toxicants, thereby exerting adverse effects on human health.³ The catalyzed diesel particulate filter (CDPF) technique,⁴ renowned for its effectiveness in soot removal, heavily relies on the activity of coated catalysts to achieve optimal purification efficiency. To date, various high-efficiency catalysts have been successfully developed, including precious metal nanoparticles,⁵ transition or alkali metal oxides,^{6,7} and rare earth metal oxides.⁸ It is worth noting that despite superior activity, the exorbitant cost of precious metal catalysts limits their application. Therefore, it is necessary to develop catalysts with desirable economic feasibility and exceptional catalytic performance for efficient soot purification.

The perovskite-type metal oxides as promising candidates have attracted much attention, owing to their good catalytic activity, versatile chemical tailoring capabilities, remarkable structural stability, etc.^{9–11} Among them, SrTiO_3 has exhibited good potential for application in heterogeneous catalytic reactions,¹² such as soot catalytic combustion,¹³ due to its

excellent thermal stability and oxidative properties. Additionally, incorporating alkali metal ions (such as Na^+ , K^+ , and Cs^+) into perovskite-type oxides can effectively enhance catalytic activity in soot combustion by promoting the activation of oxygen species.¹⁴ Significantly, the report indicates that K^+ and Sr^{2+} have a similar ion polarization effect, resulting in an even delocalization of defect charge around the saddle points in SrTiO_3 .¹⁵ Consequently, the doping of K^+ will have minimal effect on the shallow state of defects, wherein thermal ionization of defect charges easily occurs,¹⁶ a crucial aspect in thermal-catalytic oxidation reactions. These inherent properties establish K^+ as the more suitable choice, but the poor hydrothermal stability limits its application.¹⁷ Besides, the detailed catalytic mechanism associated with K^+ -related perovskite oxides in soot combustion remains undisclosed.

Received: October 13, 2024

Revised: December 13, 2024

Accepted: December 20, 2024

Published: December 26, 2024



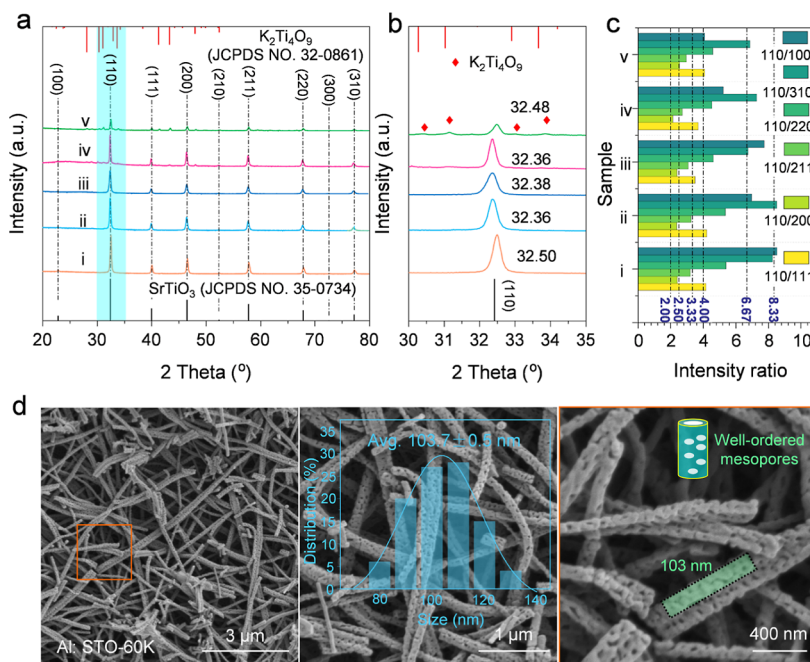


Figure 1. (a) XRD patterns of the as-prepared catalysts [(i) Al:STO; (ii) Al:STO-20K; (iii) Al:STO-40K; (iv) Al:STO-60K; (v) Al:STO-80K]. (b) Corresponding magnified XRD patterns. (c) The relative intensity of (110) diffraction peak. (d) SEM images of Al:STO-60K.

Polycrystalline materials always exhibit an instability of phase structure under the influence of heat energy,^{18–20} resulting in K⁺ loss due to the high mobility in thermal-catalytic soot oxidation.¹⁷ Thus, developing highly ordered crystalline materials, such as single-crystalline metal oxides, is crucial for stabilizing the active components, as demonstrated by the double-perovskite metal oxides.²¹ As a typical gas-solid–solid reaction, the contact efficiency between the soot and catalyst active sites is crucial for enhancing the catalytic activity. Therefore, the construction of advanced porous structures should be considered. For example, the three-dimensional ordered microporous (3DOM) catalysts with a large pore size (>200 nm) can allow soot particles (~25 nm) to enter the inner structure, significantly enhancing contact efficiency.²² Likewise, porous nanotubular catalysts are promising candidates for the efficient removal of soot due to the multiple collisions between soot and active sites within the catalyst.²³ Moreover, introducing ordered mesopores into these advanced materials can effectively promote the adsorption and further subsequent of NO,²⁴ leading to the more efficient oxidation of soot by NO₂. However, effectively integrating the single crystal characteristics and the superior porous structure of the material remains a grand challenge. Notably, the electrospinning technique is effective in promoting the formation of perovskite oxides with enhanced crystallinity,^{25,26} while Al³⁺ facilitates self-assembly and stabilization of ordered mesopores.^{27,28}

Herein, we successfully self-assemble the K-doped single-crystalline SrTi_{0.95}Al_{0.05}O₃ nanotubes with ordered mesopores using electrospinning and sol–gel techniques, assisted by an aging process. With the assistance of K⁺, high crystallinity, and an ordered mesoporous nanotubular structure, the catalysts performed remarkable catalytic performance for soot purification. The correlation between K⁺ and catalytic activity, as well as stability, was systematically investigated and discussed. Then, the origin of K⁺ promoting the soot catalytic oxidation was deeply revealed by in situ characterizations and density

functional theory (DFT) calculations. This work paves the way for developing novel catalysts utilized in thermal catalytic heterogeneous reactions.

2. MATERIALS AND EXPERIMENTAL METHODS

2.1. Catalyst Synthesis. The detailed procedures for self-assembly of ordered mesoporous perovskite-type Sr_{1-x}K_xTi_{0.95}Al_{0.05}O₃ ($x = 0, 0.2, 0.4, 0.6$, and 0.8) nanotubes with a single-crystalline structure outlined in **Section 1.1** of the Supporting Information. The obtained samples are denoted as Al:STO, Al:STO-20K, Al:STO-40K, Al:STO-60K, and Al:STO-80K, respectively.

2.2. Characterizations. The intrinsic properties of the as-prepared catalysts and characteristic properties of the reaction process were determined through a series of ex/in situ techniques and multiple electrochemistry tests. The corresponding details were introduced in **Sections 1.2** and **1.3** of the Supporting Information.

2.3. Computational Methodology. The impact of K⁺ on soot catalytic oxidation was further investigated and determined through density functional theory (DFT) calculations. The corresponding computational models and calculation settings were displayed in **Section 1.4** of the Supporting Information.

2.4. Evaluation of Catalytic Performance. The catalytic performance was evaluated by temperature-programmed oxidation of soot (soot-TPO), the activation energy (E_a), and the turnover frequency (TOF). **Section 1.5** of the Supporting Information presents the evaluation methods and details.

3. RESULTS AND DISCUSSION

3.1. Structural and Textural Properties. The main characteristic peaks of all samples, as depicted in **Figure 1a**, exhibited a strong resemblance to the standard peaks of cubic-phase perovskite SrTiO₃ (JCPDS No. 35-0734). Notably, the

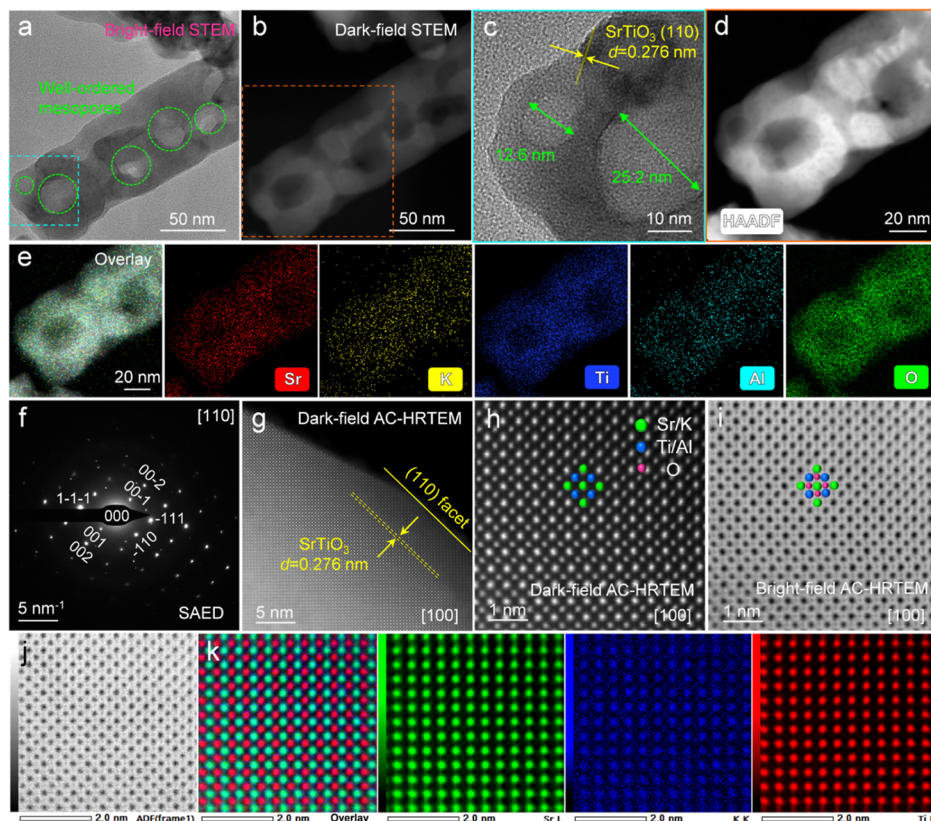


Figure 2. (a,b) TEM images of Al:STO-60K. (c) HRTEM image of Al:STO-60K. (d,e) HAADF image and the corresponding EDS element mapping images of Al:STO-60K. (f) Selected-area electron diffraction (SAED) pattern image of Al:STO-60K. (g–i) AC-HRTEM images of Al:STO-60K. (j,k) Atomic HRTEM image and the corresponding atomic EDS element mapping images of Al:STO-60K obtained from [110] zone axis.

characteristic diffraction peaks associated with $K_2Ti_4O_9$ (JCPDS No. 32-0861) can be detected in Al:STO-80K, indicating a phase transfer within the $SrTiO_3$ crystal due to an increased introduction of K^+ ions. Meanwhile, the corresponding magnified XRD patterns were additionally presented in Figure 1b. An increase in the d value leads to a negative shift in the diffraction angle of the (110) lattice fringe, implying that K^+ ions predominantly contribute to the contraction of the cubic-phase $SrTiO_3$ lattice. The larger radius of K^+ (1.64 \AA) compared to Sr^{2+} (1.44 \AA), when coordinated with 12 O^{2-} in $SrTiO_3$, primarily accounts for this phenomenon. Specifically, the phase transfer in Al:STO-80K facilitates the influx of K^+ ions into $K_2Ti_4O_9$ rather than $SrTiO_3$, thereby inducing a positive shift in the (110) diffraction peak. The relative intensity ratios of (110)/(111), (110)/(200), (110)/(211), (110)/(220), and (110)/(310) exhibit a noticeable increase compared to the standard values of 2.00, 3.33, 2.50, 4.00, and 6.67, as shown in Figure 1c, indicating the exposure of (110) facets during the crystal growth of nanoparticles in nanotubes. Moreover, the relative intensity ratio of (110)/(100) exhibits a significant reduction compared to the standard value of 8.33, indicating an increased exposure of the (100) facet in conjunction with the exposure of the (110) facet. As seen from the SEM images of Al:STO in Figure 1d, the nanotubes aggregate into a well-connected network, exhibiting an average size of 103.7 nm with a narrow distribution, indicating their homogeneous characteristics. Besides, the measured average length of broken nanotubes is approximately $1.14\text{ }\mu\text{m}$ (Figure S1), performing an aspect ratio of 11.07. Additionally,

significant proportion of self-assembled mesopores present remarkable surface regularity on nanotubes, mainly influenced by the aging processes. Furthermore, comparable outcomes can be derived from the SEM images of other samples (Figure S2). In particular, some nanorods associated with $K_2Ti_4O_9$ caused by the excessive introduction of K^+ ions are captured in Figure S3.

As seen from the bright-field STEM images (Figures 2a and S4a) and dark-field STEM images (Figures 2b and S4b,c) demonstrate the successful self-assembled of well-ordered mesopores on the surface of Al:STO-60K. As evidenced in previous studies,^{27,29} the acetic acid's acetate groups can easily substitute hydroxyl groups of metal alcoholates. Meanwhile, their bidentate nature enables direct chelation or bridging with metal ions, leading to a pronounced decrease in their reactivity toward H_2O , which is advantageous for controlling particle size and condensation kinetics. By subjecting the framework to an extended aging process, the intensified condensation facilitates the preservation of the initial mesoporous structure after calcination. Moreover, the HRTEM image of Al:STO-60K is presented in Figure 2c, showing the characteristic d value of (110) lattice fringe for perovskite-type $SrTiO_3$ to be 0.276 nm , consistent with XRD measurements using the Scherrer formula. It further suggests the successful preparation of cubic-phase $SrTiO_3$ perovskite and the well-defined exposure of (110) facets. Meanwhile, the typical mesopores (Figure 2c) exhibit a calibrated size of approximately 12.6 and 25.2 nm , demonstrating a regular channel structure and detailing the ordered mesoscopic properties. Figure 2d displays the HAADF

image of Al:STO-60K corresponding to the red area in Figure 2b, and the associated EDS element mapping images (Sr, K, Ti, Al, and O) are depicted in Figure 2e. The well-organized atomic-level arrangement of perovskite contributes to the relatively uniform distribution within the nanotubes. In addition, the SAED pattern image of Al:STO-60K is obtained from the [110] zone axis and performed in Figures 2f and S5, illustrating its single crystalline property. Besides, the dark-field AC-HRTEM image in Figure 2g displays the exposure of (110) facets in the [100] zone axis, indicating successful facet engineering achieved through impurity metal ion doping. As renowned, the surfaces of (100) and (110) facets are respectively rich in holes and electrons for SrTiO₃ crystal, preferentially and effectively driving the transfer of free electrons to the (100) facets.¹⁰ Meanwhile, the (100) facets exhibit higher activity in catalysis reactions than the (110) facets for SrTiO₃ crystal, further confirming their dominant influence in the catalytic oxidation of soot.^{30,31} The AC-HRTEM images captured in dark and bright fields, as performed in Figure 2h,i, provide the detailed atomic arrangements of diverse elements within Al:STO-60K. In comparison, the A-site metal ions in perovskite, such as Sr²⁺ and K⁺, are characterized by their larger atomic size with a brighter display. In contrast, the B-site metal ions, including Ti⁴⁺ (or Ti³⁺) and Al³⁺, exhibit a darker and smaller appearance. The O²⁻ species is notably observed to be well positioned between the metal ions. According to the atomic force microscope (AFM) images in Figures 2j and S4d, the corresponding atomic EDS element mapping images of Al:STO-60K are obtained from the [100] zone axis and presented in Figures 2k and S4e–h. Moreover, Figure S6a demonstrates the absence of Al³⁺ in the line profile corresponding to the A site (Sr²⁺). In contrast, the line profile in Figure S6b exhibits clear evidence of Al³⁺ presence at the B site (Ti³⁺ or Ti⁴⁺). Consequently, the determined atomic arrangements exhibit remarkable conformity with the structural properties manifested by cubic-phase SrTiO₃ crystal.

As obtained from the HRTEM images (Figure S7a,c), the *d* value of (110) lattice fringe (2.76 Å) calibrated in the corresponding IFFT images (Figure S7b,d) illustrates the characterization of cubic-phase SrTiO₃. Meanwhile, the SAED image obtained from the [100] zone axis (Figure S7e) confirms the single crystalline property of SrTiO₃ in Al:STO-80K. As seen in Figure S7f, the HAADF images display relatively irregular mesopores in circular morphology, which may be attributed to the phase transition from cubic SrTiO₃ to monoclinic K₂Ti₄O₉. As shown in Figure S7g, the cubic-phase SrTiO₃ in Al:STO-80K also exhibits a homogeneous distribution of elements, similar to that observed in Al:STO-60K. In addition, the TEM images in Figure S8a,b showcase the presence of monoclinic K₂Ti₄O₉ nanorods within Al:STO-80K with a typical width of approximately 120 nm. This determination is based on the characteristic *d* values of (310) facets (3.2 Å) and (200) facets (8.8 Å), as figured out in the HRTEM images (Figure S8c–g) and corresponding IFFT image (Figure S8h). The SAED image of K₂Ti₄O₉ nanorods (Figure S8i) highlights their single-crystal characteristics, thereby providing further evidence for the single crystalline property in Al:STO-80K. As obtained from Figure S8j, the elements mapping images (Sr, K, Ti, Al, and O) in Figure S8k–p reveal their uniform distribution with a decreased concentration of Sr²⁺ within K₂Ti₄O₉. Moreover, as observed from Figure S9, all samples display type II N₂ adsorption–

desorption isotherms and H3-type hysteresis loops within the range of 0.9–1.0 (P/P_0). Meanwhile, in comparison within this region, Al:STO-80K demonstrates a notably diminished increase in adsorption volume relative to others upon increasing the relative pressure, suggesting the occurrence of mesopore or nanovoid destruction on the walls induced by phase transition.²³ The lower specific surface area (4.813 m² g⁻¹) and total pore volume (0.013 cm³ g⁻¹) of Al:STO-80K, as presented in Table S1, provide further evidence for this finding. Besides, the small H2-type hysteresis loops ranging from 0.2 to 0.9 (P/P_0) in all samples imply the presence of mesopores or nanovoids. Particularly, the isotherms in the low-pressure region of the middle section exhibit linear characteristics attributed to the unrestricted mono- or multilayer adsorption taking place within particle-accumulated macropores.³² As illustrated in Figure S10, in contrast to Al:STO-80K, others display more prominent peaks in the 10–40 nm mesoporous feature range, further substantiating the size of well-ordered mesopores and the disappearance induced by phase transition.

3.2. Catalyst Surface State and Redox Properties. The XPS survey spectra reveal distinct peaks corresponding to the characteristic Sr 3d, Ti 2p, and O 1s states, as illustrated in Figure S11a. The high-resolution K 2p spectra shown in Figure S11b provide evidence for successfully incorporating K⁺ ions into the SrTiO₃ crystal, with the peak observed in the K 2p_{3/2} region at approximately 292.4 eV. The high-resolution Sr 3d spectra in Figure S11c perform the peaks located at 134.8 and 133.9 eV in the Sr 3d_{3/2} region, attributed to Sr-based suboxides and perovskites, respectively.³³ Figure S12 shows the high-resolution spectra of O 1s and Ti 2p, while Tables S2 and S3 display the corresponding deconvolution results. The deconvoluted profiles exhibiting peaks at approximately 531.0 eV can be ascribable to the active oxygen species (O_{ads}), and the peaks observed around 529.40 eV demonstrate the lattice oxygen species (O_{lat}).³⁴ As renowned, the O_{ads} are highly related to oxygen vacancies (O_v) containing free electrons, resulting from the liberation of O_{lat} in the form of O₂.³⁵ As evident, the doping of low-valence K⁺ in Al:STO-20K results in an enhanced R1 (O_{ads}/O_{lat}) value (0.70) compared to Al:STO (0.55), indicating its facilitation of oxygen activation within the formed O_v by the free electrons. Meanwhile, the R2 (Ti³⁺/Ti⁴⁺) value of Al:STO-20K (0.282) is comparatively higher than that of Al:STO (0.254), suggesting the potential localization of excess free electrons by Ti⁴⁺, resulting in the formation of Ti³⁺ species. Consequently, the free electrons enable simultaneous activation of O₂ to form O_{ads} and reduction of Ti⁴⁺ to Ti³⁺. Notably, the concentration of surficial active oxygen species remains essentially unaltered despite an increased introduction of K⁺. This phenomenon can be ascribed to the localization of free electrons centered at Ti⁴⁺ induced by structural distortion.¹⁶ In line with this finding, the relative concentration of Ti³⁺ demonstrates a significant increase (25.59%) upon the increase in K⁺ doping (below 40%), as further evidenced by the EPR results in Figure S13. The characteristic g-values of Ti³⁺ and O_v are 1.997 and 2.003, respectively.^{36,37} The higher intensity of the peaks demonstrated an increased concentration of Ti³⁺ and O_v aroused by the K⁺ doping. In contrast, when the K⁺ doping level exceeds 40%, there is a considerable increase in Ti⁴⁺ concentration, attributed to the phase transition from SrTiO₃ to K₂Ti₄O₉. Typically, Ti³⁺ defects serve as combination centers in SrTiO₃ for photoexcited carriers,^{15,38,39} thereby leading to the decrease

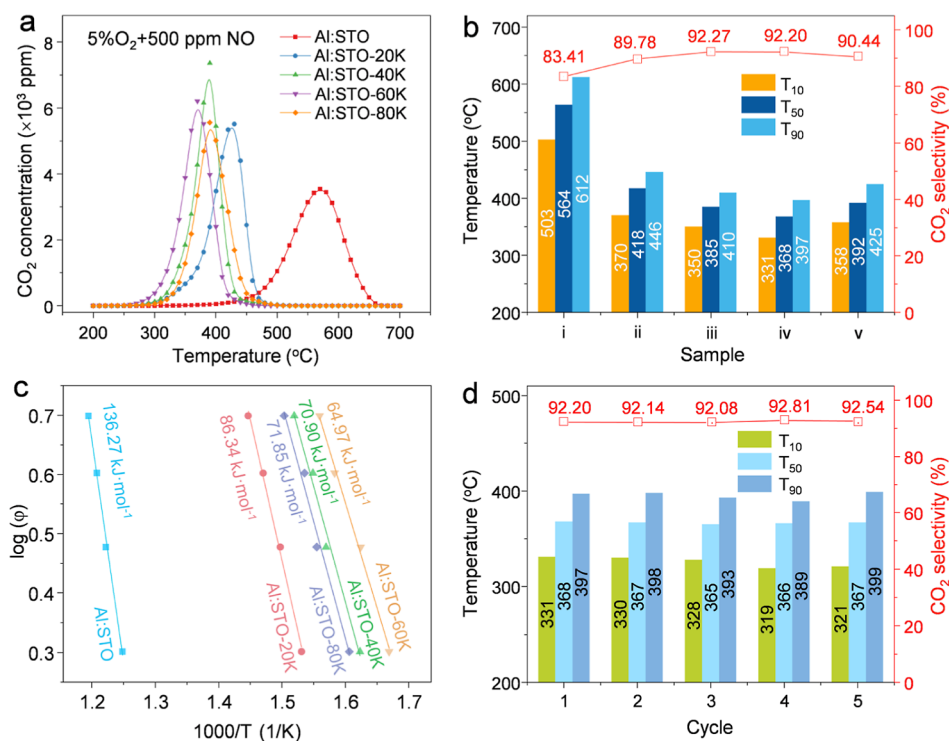


Figure 3. (a) Soot TPO profiles of the catalysts for soot combustion in the presence of O₂ (5%) and NO (500 ppm). (b) Catalytic performance of the catalysts for soot combustion. (c) Ozawa plots for soot conversion of 50% under loose contact conditions in the presence of O₂ (5%) and NO (500 ppm). (d) Performance of stability tests over Al:STO-60K.

in transient photocurrent response and increase in electrochemical impedance (Figure S14). This result provides compelling evidence for the localization of free electrons at Ti⁴⁺ sites to form Ti³⁺ induced by K⁺ doping. Based on these findings, it can be inferred that the defect charges at Ti³⁺ sites will play a pivotal role in the thermally induced oxygen activation on the surface.

The UV-vis spectra in Figure S15a reveal a significant redshift of the adsorption band edges from 376.8 to 379.2 nm upon K⁺ doping. As determined from the Tauc plots (Figure S15b), the bandgap of K-doped STO samples exhibits a decrease from 3.19 eV to approximately 2.85 eV. The discernible narrowing of the bandgap is primarily due to the enhanced concentration of O_v induced by K⁺ doping, and the bandgap of SrTiO₃ remains unaffected by K⁺.^{15,40} The bandgap narrowing will result in more densely distributed energy levels, encompassing the valence band, conduction band, and defects.⁴¹ The densification of energy levels can facilitate the thermal-driven vibration of defect charges, causing them to displace from their initial positions and accumulate in localized regions.⁴² Therefore, in addition to increasing the defect charge quantity, K⁺ can also expedite the defect-charge thermal excitation, thereby exerting a decisive influence on thermal catalytic reactions.

The increased doping of K⁺ leads to observing a small peak at 200–300 °C, as shown in Figure S16a. This phenomenon can be attributed to the reduction of active oxygen species, generated through the K⁺ facilitation. Moreover, a significant enhancement in the peak intensity at 500–700 °C is observed due to the increased K⁺ doping, while this phenomenon can be attributed to the reduction of Ti⁴⁺ to Ti³⁺. This result indicates that the structural distortion aroused by K⁺ can diminish the stability of Ti⁴⁺ within SrTiO₃ crystals and facilitate its

reduction to Ti³⁺, as confirmed by XPS analysis. Similarly, in the O₂-TPD profiles (Figure S16b), a new peak (450–550 °C) with enhanced intensity induced by K⁺ doping can be observed, which is ascribed to the reactive surface lattice oxygen (O_{lat}) along with the peak for the bulk O_{lat} at 600–700 °C.³⁴ The decreased desorption temperature of O_{lat} further supports the effect of the structural distortion on enhancing its transfer efficiency in SrTiO₃ crystals. In addition, the peak at 50–150 °C is commonly associated with the robust physical adsorption of O₂ and the adsorbed O₂⁻ species.⁴³ The peak observed at 50–150 °C for Al:STO-40K is significantly higher compared to that of Al:STO, due to the enhanced adsorption of O₂⁻ species resulting from the incorporation of K⁺ ions, thereby impeding the reduction in physical adsorption of O₂ due to a decrease in specific surface area. However, it has a decreased intensity for Al:STO-60K and Al:STO-80K, indicating a reduced specific surface area due to a phase transition. The introduction of K⁺ is primarily responsible for the enhanced peak intensity observed at 250–350 °C ascribable to the chemical adsorption of oxygen species (O⁻).⁴³ This result signifies the K⁺-induced enhancement in the capacity to activate oxygen species, specifically O₂⁻ species.

3.3. Performances for Catalytic Soot Purification. As presented in Figure S17, the T₅₀ of pure soot oxidation without catalysts was determined to be 593 °C. As seen in Figure 3a,b, the addition of catalysts significantly enhances the efficiency of soot purification, as evidenced by the T₅₀ value of Al:STO at 564 °C and a corresponding CO₂ selectivity of 83.41% (S_{CO₂}). In comparison, Al:STO-20K exhibits a significantly reduced T₅₀ (418 °C) and an increased S_{CO₂} (89.78%), highlighting the crucial role of K⁺ in facilitating soot oxidation. As the level of K⁺ doping increases, the T₅₀ value gradually decreases for Al:STO-40K (385 °C) and Al:STO-60K (368 °C) with the

CO_2 selectivity over 90.00%. However, the T_{50} value of Al:STO-80K (392°C) is higher than that of Al:STO-60K due to the limited utilization of active sites aroused by partial destruction of nanotubes. According to the TPO profiles and the T_{50} determined at different heating rates (Figure S18), the activation energy (E_a) values are calculated and presented in Figure 3c. Consistent with the catalytic performance, Al:STO-60K exhibits the lowest E_a ($64.97 \text{ kJ mol}^{-1}$) compared to Al:STO ($136.27 \text{ kJ mol}^{-1}$), Al:STO-20K ($86.34 \text{ kJ mol}^{-1}$), Al:STO-40K ($70.90 \text{ kJ mol}^{-1}$), and Al:STO-80K ($71.85 \text{ kJ mol}^{-1}$). As shown in Figure S19, within the initial temperature range of 200 – 350°C in soot-TPR profiles, the predominant oxidants involved in the reaction are the active oxygen species (O^- or O_2^-). The K^+ significantly enhances the surficial activation of oxygen species, consistent with the results of the analysis above. Moreover, the TPR profiles between 350 and 500°C suggest the participation of subsurface lattice oxygen species (O_{slat} , $\text{O}_{\text{sb}}^{2-}$) in the soot oxidation, while the part exceeding 500°C is ascribed to the effect of lattice oxygen species (O_{blat} , O^{2-}).^{44–46} The negative shifts observed in the soot profiles further demonstrate the influence of K^+ on inducing structural distortion, thereby promoting the transfer of lattice oxygen.

As displayed in Figure S20a, the reaction rates are determined to be $2.79 \times 10^{-7} \text{ mmol s}^{-1}$ (Al:STO-20K), $5.49 \times 10^{-7} \text{ mmol s}^{-1}$ (Al:STO-40K), $8.32 \times 10^{-7} \text{ mmol s}^{-1}$ (Al:STO-60K), and $7.30 \times 10^{-7} \text{ mmol s}^{-1}$ (Al:STO-80K), respectively. Figure S20b displays a linear relationship between the reaction rates and the K content, further illustrating the effect of K^+ as active sites. Therefore, as shown in Figure S20c, the TOF_K values exhibit proximity, which are 0.019 h^{-1} (Al:STO-20K), 0.018 h^{-1} (Al:STO-40K), and 0.017 h^{-1} (Al:STO-60K). As evidenced by BET results, with the enhancement in K^+ doping ($\sim 60\%$), the specific surface area exhibits a significant decrease, potentially attributed to the reduction of mesopores. Consequently, it may weaken the adsorption and activation of O_2 and NO , potentially resulting in a decline in catalytic activity. However, the Brownian-like motion will contribute to the multiple collisions in the nanotube with enhanced contact efficiency between soot and active sites (K^+) on the catalyst surface,²³ as depicted in Figure S20d. Therefore, the Brownian-like motion mitigates the impact of mesopore misses on the activity, as indicated by the closely aligned TOF_K values. As illustrated in Figure S20d, the doping of K^+ at 80% notably induces a structural transformation from nanotubes to nanorods. The absence of Brownian-like motion leads to a significant decrease in the TOF_K value (0.010 h^{-1}), indicating a reduced utilization efficiency of active sites (K^+) due to the decline in mesopores and consequent reduction in specific surface area. In summary, in the presence of a mesoporous nanotubular structure, the catalytic activity is primarily improved by the extent of K^+ doping.

As shown in Figure S21a, The T_{50} of Al:STO-60K remains unchanged after 6 recycle tests, indicating a stable activity. Meanwhile, the SEM and TEM images in Figure S21b further substantiate the desirable structural stability of the catalyst. We also conducted isothermal reactions at 300°C to investigate the hydrothermal stability of Al:STO-60K in the presence of 10% H_2O vapor, 5% O_2 , and 500 ppm of NO , considering that diesel engine exhaust gas temperatures typically range between 150 and 400°C .⁴⁷ As shown in Figure S22a,b, the activity of Al:STO-60K decreases linearly throughout 5 recycling tests,

directly proportional to the catalyst's quality. The observed decrease in activity primarily results from catalyst mass loss rather than K^+ loss during each cycle, which is caused by inevitable degradation due to human and system-related factors. Moreover, we also kept Al:STO-60K in the liquid boiling water (100°C) for 3 h to investigate the K^+ loss. As shown in Figure S22c, $1.87 \text{ mmol L}^{-1} \text{ K}^+$ and $0.68 \times 10^{-4} \text{ mmol L}^{-1} \text{ Sr}^{2+}$ can be detected in the H_2O after filtering, indicating the significant loss of K^+ at this demanding condition, as further demonstrated by the decrease from 0.5724 to 0.5091 in the $\text{K}/(\text{Sr} + \text{K})$ value. Notably, the Al:STO-60K after hydrothermal stability tests shows slight differences in K^+ content (0.5707) compared to the fresh sample (0.5724) observed in Figure S22d and Table S8, confirming the good stability of K^+ in STO exposed in H_2O vapor. By comparison, we found that the catalyst exhibits good hydrothermal stability at conditions comparable to diesel engine exhaust gas, instead of being immersed in a liquid medium.

As illustrated in Figure S23a, compared to single-crystalline STO, enhancement in element or ion movement in polycrystalline STO can be facilitated by metastable crystal phases during the thermal catalytic reaction.⁴⁸ It will promote the flow of K^+ in STO due to the weak bond energy, finally resulting in the easier loss of K^+ exposed in H_2O vapor.¹⁷ In comparison, the stable phase structure of single-crystalline STO leads to strong bond energy, thus enhancing the stabilization of K^+ . As demonstrated in Figure S27, the active (100) facet prefers to expose Ti–O layers due to the more stable system. Therefore, as shown in Figure S23b, the Ti–O layers can decrease the exposure of the K–O layers in the H_2O vapor, suppressing the K^+ loss. These characteristics may contribute to the good hydrothermal stability of Al:STO-60K.

At T_{50} , the selectivity to CO_2 is lower than 93% indicating incomplete soot combustion. This phenomenon may be attributed to the mismatch between the capacity for activation or transfer of active oxygen species and the rate of catalytic combustion at the temperature of T_{50} .⁴⁹ Notably, the CO_2 selectivity around initiative temperature (T_{10}) is consistently prioritized for evaluating catalysts and is significant for soot combustion in real conditions,⁵⁰ due to the exhaust gas temperatures (150 – 400°C). Therefore, we investigated the isothermal reaction of soot catalytic oxidation at 300°C close to T_{10} without H_2O vapor. As shown in Figure S23c, Al:STO-60K exhibits an increased CO_2 selectivity reaching 98.38%, indicating that the activation efficiency of active oxygen species prefers to match the rate of catalytic combustion at 300°C . In addition, as shown in Figure S23d, the selectivity of CO_2 for Al:STO-60K in the hydrothermal stability tests remarkably reaches 100% with enhanced production, meeting the requirements of real conditions of CDPF. This result suggests the potential effect of H_2O vapor on the wetting conditions of the soot–catalysts interface for improving their contact efficiency, thereby facilitating the oxygen mobility and transfer, and subsequent soot oxidation.⁵¹ Meanwhile, the H_2O molecules can also act as a cocatalyst, promoting the formation of oxygen-containing byproducts like oxygenic complexes, nitric acid, or nitrous acid on the surface of soot through reactions between carbon and NO_2 .⁵² This also can enhance the efficiency of soot oxidation.

3.4. Insight into the Mechanism for Catalytic Soot Purification. The in situ XPS survey spectra in Figures S24a and S25a reveal the presence of peaks corresponding to O 1s,

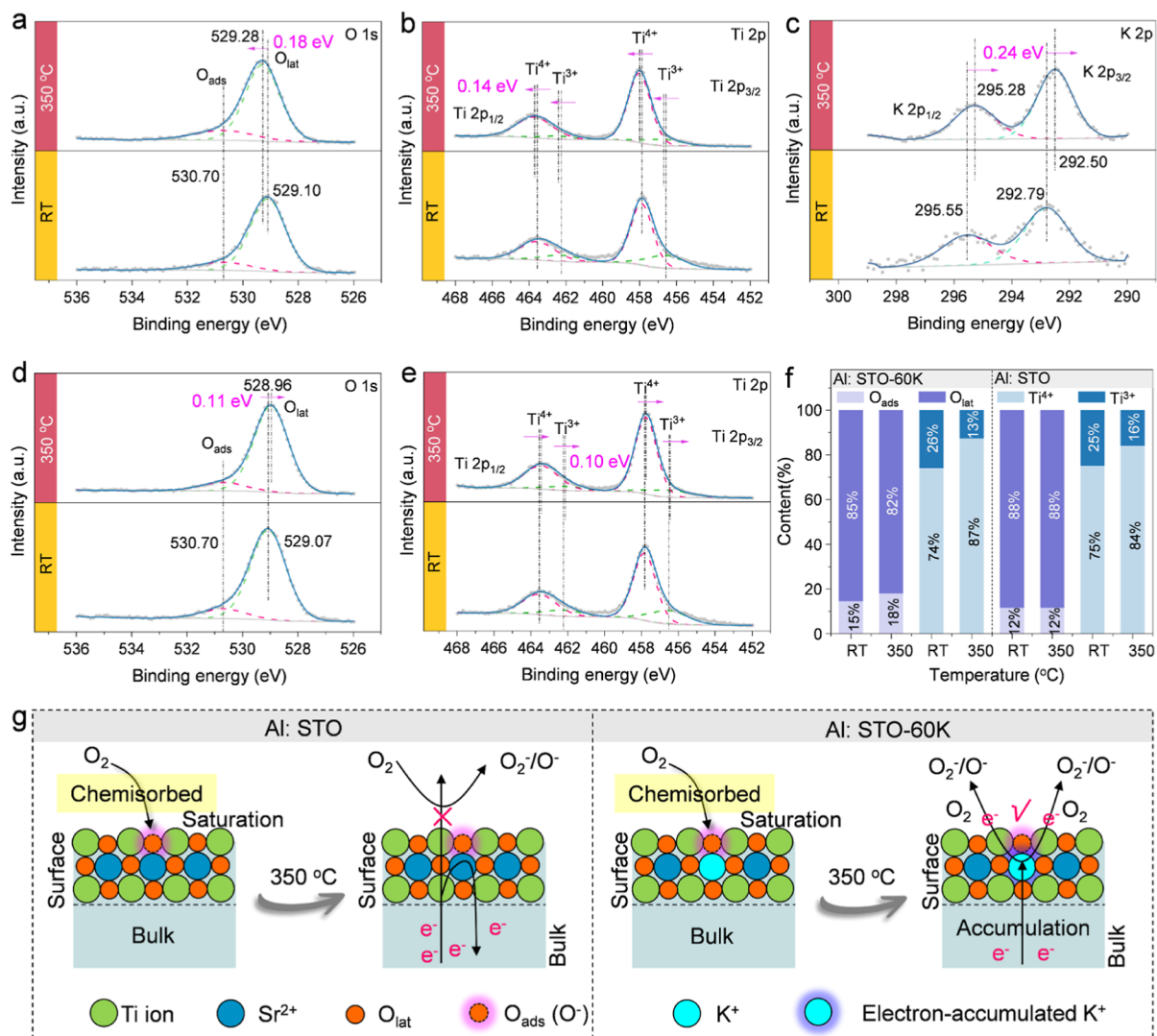


Figure 4. In situ high-resolution XPS spectra for Al:STO-60K: (a) O 1s; (b) Ti 2p; (c) K 2p. In situ high-resolution XPS spectra for Al:STO: (d) O 1s; (e) Ti 2p. (f) The obtained content of oxygen species and titanium species from in situ high-resolution XPS spectra. (g) Illustration of the electron accumulation and accelerated activation of O₂ affected by K⁺ during thermal catalysis.

Ti 2p, C 1s, and Sr 3d at room temperature (RT) and 350 °C (350). The absence of shifts in the peaks for Al 2p, as observed in Figures S24b and S25b after heating to 350 °C, suggests that it has a minimal impact on charge transfer during the reaction. Meanwhile, the peak positions of Sr-based suboxides and SrO in perovskite remain unchanged with closely relative ratios (R3) even after heating to 350 °C, as shown in Figures S24c and S25c, and Table S4. This observation confirms that Sr-based species also do not influence charge transfer during the reaction. As depicted in Figure 4a, for Al:STO-60K, the peak position of lattice oxygen (O_{lat}) shows a positive shift from 529.10 to 529.28 eV, indicating the migration of defect charge from O_{lat} during the reaction. The O_{ads} content increases from 15% (RT) to 18% (350) in Figure 4f, derived from the R4 values (O_{ads}/O_{lat}) as shown in Table S5, implying the involvement of the defect charge in oxygen activation. Moreover, the positions of the peaks attributed to Ti³⁺ and Ti⁴⁺ exhibit prominent positive shifts (0.14 eV), while the R5 value (Ti⁴⁺/Ti³⁺) increases from 2.86 to 6.91, as illustrated in Figure 4b and Table S6. These findings suggest that the defect charge originates from Ti³⁺ sites and transfers to O_{ads} through Ti ions under thermal stimulation. Notably, as shown in Figure

4c, the observed negative shifts (0.24 eV) of the peaks in high-resolution XPS spectra of K 2p indicate the accumulation of defect charge at K⁺ sites during thermal catalytic reaction. Consequently, in conjunction with the UV-vis findings, it can be inferred that K⁺ sites within SrTiO₃ crystals serve as localized regions for charge accumulation. In contrast, Al:STO demonstrates negative shifts (0.11 eV) of the peaks for the oxygen species during the reaction, while maintaining the same O_{ads} (12%) and O_{lat} contents (88%) as shown in Figure 4d, which are calculated based on the R4 values shown in Table S5. In addition, the Ti³⁺ content decreases from 25% (RT) to 16% (350) in Figure 4f, as determined based on the R5 values in Table S6. Besides, Figure 4e shows negative shifts (0.10 eV) in the peaks for both Ti³⁺ and Ti⁴⁺. Based on the obtained results for Al:STO, it can be inferred that at room temperature, O₂ tends to chemisorb onto O_v until reaching saturation as illustrated in Figure 4g. However, the thermal-driven defect charge cannot be utilized for O₂ activation due to the saturated adsorption of surface O_v without any additional formation of O_v on the surface, which necessitates higher energy levels. Therefore, the defect charge will flow back to the bulks in SrTiO₃ crystals, contributing to the negative shifts in peaks

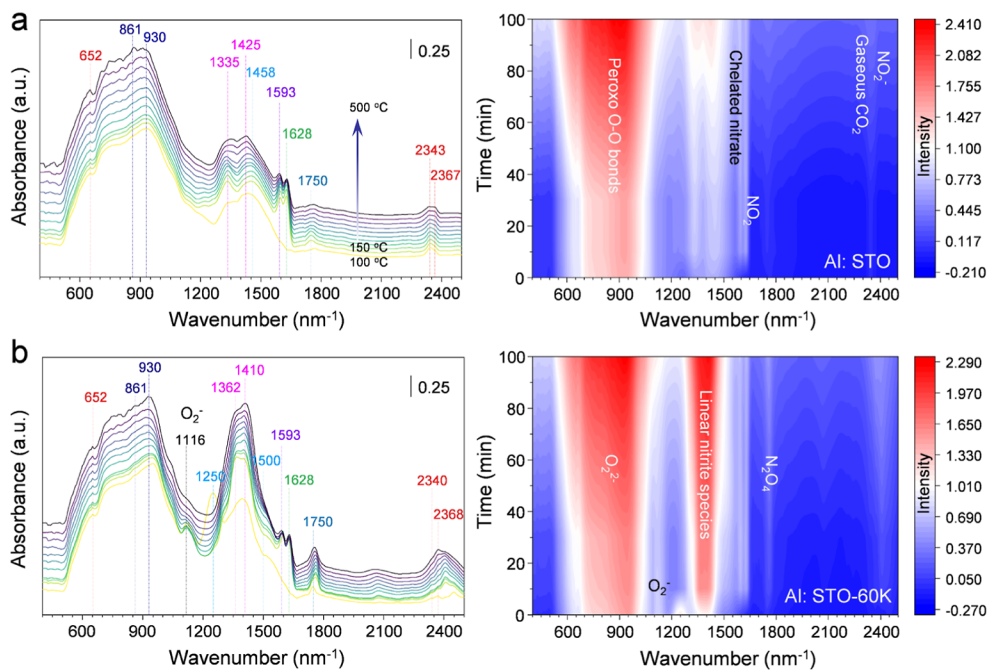


Figure 5. In situ DRIFTS spectra for the catalytic reversion of NO (500 ppm) in the presence of 5% O₂ over Al:STO (a) and Al:STO-60K (b).

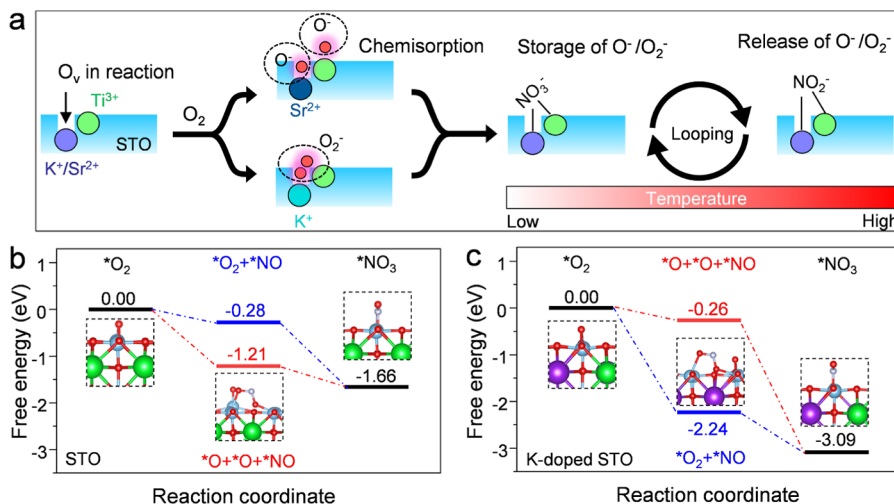


Figure 6. (a) Storage and release mechanism of active oxygen species for soot catalytic oxidation in the presence of NO and O₂. (b) and (c) Calculated potential energy profiles based on the relevant adsorption Gibbs free energy on (100) surface of STO and K-doped STO.

associated with O_{lat} and Ti ions. Compared to Al:STO, the K⁺-induced structural distortion in Al:STO-60K can facilitate the formation of surface O_v during heat treatment by reducing the energy barrier, offering additional sites for O₂ activation. Moreover, K⁺ can effectively serve as a charge accumulation center, leading to a substantial decrease in the transfer energy of defect charge and facilitating the proficient activation of O₂ at O_v sites.

As illustrated in Figure 5a,b, in the in situ DRIFTS spectra of Al:STO and Al:STO-60K, the peaks observed at approximately 652 and 2340 cm⁻¹ can be attributed to the bending vibration and symmetrical stretching vibration of CO₂ molecules, respectively.⁵³ The temperature-dependent increase in CO₂ vibration peak intensity for Al:STO can be attributed to its desorption, indicating the presence of superior mesoporous structures within the catalysts. The peaks at 861 and 930 cm⁻¹ can be ascribed to the stretching of the peroxy O–O bonds,⁵⁴

such as the O₂²⁻ species.⁵⁵ Notably, in contrast to Al:STO, the spectrum of Al:STO-60K exhibits a distinct peak at 1116 cm⁻¹ attributed to the O₂⁻ species, which is consistent with the findings from O₂-TPD. These results demonstrate the influence of K⁺ on the modulation of key active oxygen species involved in the reaction. Besides, the peak intensity of O₂⁻ decreases as the temperature rises and a stable peak at 1628 and 1750 cm⁻¹ attributed to NO₂ and N₂O₄ can be detected,^{56,57} indicating NO oxidation by active oxygen species. The peaks at approximately 1458 and 1593 cm⁻¹ can be ascribed to the linear, chelated nitrate species, while the peak at 1250 cm⁻¹ is associated with the mo-NO₃⁻.⁵⁶ As depicted in Figure S26, the peaks at 2888 and 2920 cm⁻¹ can be attributed to the bi-NO₃⁻ and br-NO₃⁻.⁵⁸ These findings demonstrate the formation of KNO₃ or SrNO₃ on the surface through the combination of active oxygen species, NO, and metal ions. Moreover, both samples exhibit peaks at

approximately 1362 and 1425 cm⁻¹ due to the formation of linear nitrite species.⁵⁹ Meanwhile, the peak at approximately 2367 cm⁻¹ is also corresponding to the generation of NO₂⁻.⁵⁸ As observed, the peaks of nitrite species exhibit enhanced intensity while the peak intensity of nitrate species decreases at elevated temperatures, implying the decomposition of nitrates into nitrites. Based on these findings, a mechanism for the storage and liberation of active oxygen mechanism centered at nitrates can be proposed, as shown in Figure 6a. Compared to Al:STO, the enhanced relative differences in the intensity of DRIFTS spectra for Al:STO-60K imply a superior capacity for storing and releasing active oxygen species.

Moreover, DFT calculations were performed to reveal the origin of K⁺ for promoting the soot catalytic oxidation in the presence of NO and O₂. Due to the exposure of (100) facets with higher activity, which can attract thermal-driven electrons, leading to their focus research in DFT calculations. As depicted in Figure S27, the model with an exposed TiO₂ layer exhibits a lower system energy (-667.89 eV) compared to another model featuring an exposed SrO/K₂O layer (-666.82 eV), indicating a more stable state that is better suited for investigation. As displayed in Figures S28a,b, the chemisorption energy of O₂ for STO is -3.96 eV much lower than -0.11 eV (K-doped STO), indicating the enhanced interaction between O_v and O₂. The higher Bader charge of the chemisorbed O₂ for STO (-0.72 and 0.51) compared to K-doped STO (-0.46 and -0.26), as shown in Table S7 and Figure S28c,d, provides further evidence supporting this finding. It can be inferred that STO exhibits higher bonding energy with the O atom of O₂ filled in O_v, further demonstrated by its higher formation energy of O_v (20.33 eV) than that of K-doped STO (15.32 eV), as shown in Figure S29. These results strongly suggest that upon the surface activation of O₂, STO is more inclined to cleave the O–O bond than K-doped STO. Therefore, as elucidated in Figures 6b and S30, STO exhibits reduced ΔG (-1.21 eV) for *NO adsorption on the surface when considering broken active oxygen species (*O+*O), compared to unbroken ones (*O₂) with the ΔG of -0.28 eV. In contrast, as shown in Figures 6c and S29 for K-doped STO, the unbroken active oxygen species (*O₂) exhibit a significantly reduced ΔG (-2.24 eV), compared to that of the broken ones (*O + *O) (-0.26 eV). The shift observed in K⁺ ion-mediated oxygen activation from *O + *O to *O₂ aligns with the findings obtained from O₂-TPD and *in situ* DRIFTS, demonstrating that K⁺ ions significantly enhance the specific activation of O_v species. Moreover, by comparison in Figure S31, in different models (*O + *O or *O₂) for adsorbing NO, both STO and K-doped STO exhibit the equivalent charge quantity transferred to NO, approximately 0.100e and 0.032e, respectively. Therefore, the significant disparities in ΔG for *NO adsorption in different models indicate distinct steric hindrance effects of the oxygen species on it. Due to this weaker effect, K-doped STO exhibits an enhanced *NO adsorption capacity ($\Delta G = -2.24$ eV) compared to STO ($\Delta G = -1.21$ eV), albeit with a lower charge quantity transferred to NO (0.032e). These results provide compelling evidence for the crucial role of K⁺ in shifting the preferred adsorption from *O + *O to *O₂, thereby facilitating the adsorption of *NO, which can act as the rate-determining step (RDS). As a result, K-doped STO exhibits significantly reduced ΔG (-3.09 eV) compared to the STO (-1.66 eV) for forming *NO₃.

4. CONCLUSION

A novel strategy for constructing single-crystalline materials integrated with ordered mesoporous nanotubes to stabilize active components and enhance mass transfer was exploited, addressing the challenge in the environmental materials associated with thermal catalysis. The electrospinning technique and aging process enable the successful synthesis of ordered mesoporous K-doped single-crystalline SrTi_{0.95}Al_{0.05}O₃ nanotubes, demonstrating excellent and stable performance for catalytic soot oxidation. In addition, new insights into the K-assistant catalytic mechanism were elucidated in detail. It is revealed that K⁺ serves as the charge accumulation and facilitates the formation of O_v by inducing structural distortion, resulting in an enhanced capacity for oxygen activation in reaction. Besides, K⁺ shifts the active species from *O to *O₂, effectively augmenting the interaction between STO and *NO, and contributing to the enhanced capability of oxygen species storage and release centered at the KNO₃. Overall, this work will offer novel insights into the development of advanced heterogeneous catalysts applied in the environmental catalytic community.

■ ASSOCIATED CONTENT

SI Supporting Information

The Supporting Information is available free of charge at <https://pubs.acs.org/doi/10.1021/acscatal.4c06289>.

Detailed synthesis information on catalysts, detailed information on characterizations, detailed information on electrochemical tests, computational methodology, evaluation of catalytic performance, additional figures and tables (PDF)

■ AUTHOR INFORMATION

Corresponding Authors

Fan Fang – Laboratory for Catalysis Engineering, School of Chemical and Biomolecular Engineering & Sydney Nano Institute, The University of Sydney, Darlington, New South Wales 2008, Australia; School of Engineering, Macquarie University, Sydney, New South Wales 2109, Australia; College of Materials Science and Technology, Nanjing University of Aeronautics and Astronautics, Nanjing 210016, PR China;  orcid.org/0000-0002-1208-1528; Email: fangfan1990@nuaa.edu.cn

Nengjie Feng – State Key Laboratory of Materials-Oriented Chemical Engineering, College of Chemical Engineering, Jiangsu National Synergetic Innovation Center for Advanced Materials, Jiangsu Collaborative Innovation Center for Advanced Inorganic Function Composites, Nanjing Tech University, Nanjing 210009, PR China;  orcid.org/0000-0001-7058-2534; Email: fengnengjie@njtech.edu.cn

Jun Huang – Laboratory for Catalysis Engineering, School of Chemical and Biomolecular Engineering & Sydney Nano Institute, The University of Sydney, Darlington, New South Wales 2008, Australia;  orcid.org/0000-0001-8704-605X; Email: jun.huang@sydney.edu.au

Authors

Fang Xu – State Key Laboratory of Materials-Oriented Chemical Engineering, College of Chemical Engineering, Jiangsu National Synergetic Innovation Center for Advanced Materials, Jiangsu Collaborative Innovation Center for Advanced Inorganic Function Composites, Nanjing Tech

University, Nanjing 210009, PR China;  orcid.org/0000-0001-9367-0334

Xue Li – State Key Laboratory of Materials-Oriented Chemical Engineering, College of Chemical Engineering, Jiangsu National Synergetic Innovation Center for Advanced Materials, Jiangsu Collaborative Innovation Center for Advanced Inorganic Function Composites, Nanjing Tech University, Nanjing 210009, PR China

Chong Chen – College of Materials Science and Technology, Nanjing University of Aeronautics and Astronautics, Nanjing 210016, PR China;  orcid.org/0000-0002-7735-2691

Yijiao Jiang – School of Engineering, Macquarie University, Sydney, New South Wales 2109, Australia;  orcid.org/0000-0002-6191-9825

Complete contact information is available at:
<https://pubs.acs.org/10.1021/acscatal.4c06289>

Author Contributions

The manuscript was written through contributions of all authors. All authors have given approval to the final version of the manuscript.

Notes

The authors declare no competing financial interest.

ACKNOWLEDGMENTS

This work was supported by the National Natural Science Foundation of China (no. 22308163), the Key Research and Development Program of Anhui Province (2022l07020035), and the Australian Research Council (LP200200615).

REFERENCES

- (1) Mei, X.; Zhu, X.; Zhang, Y.; Zhang, Z.; Zhong, Z.; Xin, Y.; Zhang, J. Decreasing the catalytic ignition temperature of diesel soot using electrified conductive oxide catalysts. *Nat. Catal.* **2021**, *4* (12), 1002–1011.
- (2) Sun, H.; Zhang, F.; Liu, S.; Liu, Y.; Zhu, B.; Yu, X.; Xie, Z.; Zhao, Z. Insight into the Synergetic Effects of NTP-La_{1-x}Ag_xMnO₃ on Soot Oxidation at Low Temperatures. *ACS Catal.* **2024**, *14*, 4927–4943.
- (3) Leni, Z.; Ess, M. N.; Keller, A.; Allan, J. D.; Hellén, H.; Saarnio, K.; Williams, K. R.; Brown, A. S.; Salathe, M.; Baumlin, N.; et al. Role of secondary organic matter on soot particle toxicity in reconstituted human bronchial epithelia exposed at the air-liquid interface. *Environ. Sci. Technol.* **2022**, *56* (23), 17007–17017.
- (4) Yu, D.; Wang, L.; Zhang, C.; Peng, C.; Yu, X.; Fan, X.; Liu, B.; Li, K.; Li, Z.; Wei, Y.; et al. Alkali metals and cerium-modified La-Co-based perovskite catalysts: facile synthesis, excellent catalytic performance, and reaction mechanisms for soot combustion. *ACS Catal.* **2022**, *12* (24), 15056–15075.
- (5) Kong, J.; Song, S.; Zhao, W.; Yu, Z.; Xiang, Z.; Li, G.; Zhang, W.; An, T. Unraveling a trade-off between positive effect and poisoning mechanism of soot over low-dose PtCu/CeO₂ for simultaneously photothermocatalytic removal of VOCs and soot. *Appl. Catal., B* **2023**, *339*, 123118.
- (6) Yu, D.; Yu, X.; Zhang, C.; Wang, L.; Fan, X.; Zhao, Z.; Wei, Y.; Liu, J.; Gryboś, J.; Leszczyński, B.; et al. Layered Na₂Mn₃O₇ decorated by Cerium as the robust catalysts for efficient low temperature soot combustion. *Appl. Catal., B* **2023**, *338*, 123022.
- (7) Li, Y.; Qin, T.; Ma, Y.; Xiong, J.; Zhang, P.; Lai, K.; Liu, X.; Zhao, Z.; Liu, J.; Chen, L.; et al. Revealing active edge sites induced by oriented lattice bending of Co-CeO₂ nanosheets for boosting auto-exhaust soot oxidation. *J. Catal.* **2023**, *421*, 351–364.
- (8) Sellers-Anton, B.; Bailon-Garcia, E.; Cardenas-Arenas, A.; Davo-Quinonero, A.; Lozano-Castello, D.; Bueno-Lopez, A. Enhancement of the generation and transfer of active oxygen in Ni/CeO₂ catalysts for soot combustion by controlling the Ni–ceria contact and the three-dimensional structure. *Environ. Sci. Technol.* **2020**, *54* (4), 2439–2447.
- (9) Chu, K.; Zong, W.; Xue, G.; Guo, H.; Qin, J.; Zhu, H.; Zhang, N.; Tian, Z.; Dong, H.; Miao, Y.-E.; et al. Cation substitution strategy for developing perovskite oxide with rich oxygen vacancy-mediated charge redistribution enables highly efficient nitrate electroreduction to ammonia. *J. Am. Chem. Soc.* **2023**, *145* (39), 21387–21396.
- (10) Takata, T.; Jiang, J.; Sakata, Y.; Nakabayashi, M.; Shibata, N.; Nandal, V.; Seki, K.; Hisatomi, T.; Domen, K. Photocatalytic water splitting with a quantum efficiency of almost unity. *Nature* **2020**, *581* (7809), 411–414.
- (11) Li, R.; Takata, T.; Zhang, B.; Feng, C.; Wu, Q.; Cui, C.; Zhang, Z.; Domen, K.; Li, Y. Criteria for Efficient Photocatalytic Water Splitting Revealed by Studying Carrier Dynamics in a Model Al-doped SrTiO₃ Photocatalyst. *Angew. Chem., Int. Ed.* **2023**, *62* (49), No. e202313537.
- (12) Wang, Q.; Warnan, J.; Rodríguez-Jiménez, S.; Leung, J. J.; Kalathil, S.; Andrei, V.; Domen, K.; Reisner, E. Molecularly engineered photocatalyst sheet for scalable solar formate production from carbon dioxide and water. *Nat. Energy* **2020**, *5* (9), 703–710.
- (13) Ura, B.; Trawczyński, J.; Kotarba, A.; Bieniasz, W.; Illán-Gómez, M. J.; Bueno-López, A.; López-Suárez, F. E. Effect of potassium addition on catalytic activity of SrTiO₃ catalyst for diesel soot combustion. *Appl. Catal., B* **2011**, *101* (3–4), 169–175.
- (14) Zhang, P.; Mei, X.; Zhao, X.; Xiong, J.; Li, Y.; Zhao, Z.; Wei, Y. Boosting Catalytic Purification of Soot Particles over Double Perovskite-Type La_{2-x}K_xNiCoO₆ Catalysts with an Ordered Macro-porous Structure. *Environ. Sci. Technol.* **2021**, *55* (16), 11245–11254.
- (15) Fang, F.; Su, Z.; Li, X.; Xu, F.; Lv, Y.; Sun, R.; Li, J.; Qin, Y.; Chang, K. Mechanistic Understanding of Alkali-Metal-Ion Effect on Defect State in SrTiO₃ During the Defect Engineering for Boosting Solar Water Splitting. *Adv. Funct. Mater.* **2023**, *33* (24), 2215242.
- (16) Pastor, E.; Sachs, M.; Selim, S.; Durrant, J. R.; Bakulin, A. A.; Walsh, A. Electronic defects in metal oxide photocatalysts. *Nat. Rev. Mater.* **2022**, *7* (7), 503–521.
- (17) Gálvez, M. E.; Ascaso, S.; Stelmachowski, P.; Legutko, P.; Kotarba, A.; Moliner, R.; Lázaro, M. J. Influence of the surface potassium species in Fe–K/Al₂O₃ catalysts on the soot oxidation activity in the presence of NO_x. *Appl. Catal., B* **2014**, *152*, 88–98.
- (18) McGuire, M. A.; Christianson, A. D.; Sefat, A. S.; Sales, B. C.; Lumsden, M. D.; Jin, R.; Payzant, E. A.; Mandrus, D.; Luan, Y.; Keppens, V.; et al. Phase transitions in LaFeAsO: Structural, magnetic, elastic, and transport properties, heat capacity and Mössbauer spectra. *Phys. Rev. B* **2008**, *78* (9), 094517.
- (19) Omori, T.; Kusama, T.; Kawata, S.; Ohnuma, I.; Sutou, Y.; Araki, Y.; Ishida, K.; Kainuma, R. Abnormal grain growth induced by cyclic heat treatment. *Science* **2013**, *341* (6153), 1500–1502.
- (20) Kainuma, R.; Imano, Y.; Ito, W.; Sutou, Y.; Morito, H.; Okamoto, S.; Kitakami, O.; Oikawa, K.; Fujita, A.; Kanomata, T.; et al. Magnetic-field-induced shape recovery by reverse phase transformation. *Nature* **2006**, *439* (7079), 957–960.
- (21) Sun, Y.-F.; Li, J.-H.; Zhang, Y.-Q.; Hua, B.; Luo, J.-L. Bifunctional catalyst of core-shell nanoparticles socketed on oxygen-deficient layered perovskite for soot combustion: in situ observation of synergistic dual active sites. *ACS Catal.* **2016**, *6* (4), 2710–2714.
- (22) Wei, Y.; Zhang, P.; Xiong, J.; Yu, Q.; Wu, Q.; Zhao, Z.; Liu, J. SO₂-tolerant catalytic removal of soot particles over 3D ordered macroporous Al₂O₃-supported binary Pt–Co oxide catalysts. *Environ. Sci. Technol.* **2020**, *54* (11), 6947–6956.
- (23) Fang, F.; Feng, N.; Wang, L.; Meng, J.; Liu, G.; Zhao, P.; Gao, P.; Ding, J.; Wan, H.; Guan, G. Fabrication of perovskite-type macro/mesoporous La_{1-x}K_xFeO_{3-δ} nanotubes as an efficient catalyst for soot combustion. *Appl. Catal., B* **2018**, *236*, 184–194.
- (24) Xiong, J.; Mei, X.; Liu, J.; Wei, Y.; Zhao, Z.; Xie, Z.; Li, J. Efficiently multifunctional catalysts of 3D ordered meso-macroporous Ce_{0.3}Zr_{0.7}O₂-supported PdAu@CeO₂ core-shell nanoparticles for soot oxidation: Synergetic effect of Pd–Au–CeO₂ ternary components. *Appl. Catal., B* **2019**, *251*, 247–260.

- (25) Zhao, B.; Zhang, L.; Zhen, D.; Yoo, S.; Ding, Y.; Chen, D.; Chen, Y.; Zhang, Q.; Doyle, B.; Xiong, X.; et al. A tailored double perovskite nanofiber catalyst enables ultrafast oxygen evolution. *Nat. Commun.* **2017**, *8* (1), 14586.
- (26) Fang, F.; Zhang, J.; Xiang, L.; Chen, C.; Feng, N.; Lv, Y.; Chang, K.; Huang, J. Ordering Bimetallic Cu-Pd Catalysts onto Orderly Mesoporous SrTiO₃-Crystal Nanotubular Networks for Efficient Carbon Dioxide Photoreduction. *Angew. Chem., Int. Ed.* **2024**, *63* (30), No. e202405807.
- (27) Fan, J.; Boettcher, S. W.; Stucky, G. D. Nanoparticle assembly of ordered multicomponent mesostructured metal oxides via a versatile sol-gel process. *Chem. Mater.* **2006**, *18* (26), 6391–6396.
- (28) Kuemmel, M.; Gross, D.; Boissière, C.; Smarsly, B.; Brezesinski, T.; Alouy, P. A.; Amenitsch, H.; Sanchez, C. Thermally stable nanocrystalline γ -alumina layers with highly ordered 3D mesoporosity. *Angew. Chem., Int. Ed.* **2005**, *44* (29), 4589–4592.
- (29) Boettcher, S. W.; Bartl, M. H.; Hu, J. G.; Stucky, G. D. Structural analysis of hybrid titania-based mesostructured composites. *J. Am. Chem. Soc.* **2005**, *127* (27), 9721–9730.
- (30) Heifets, E.; Eglitis, R.; Kotomin, E. A.; Maier, J.; Borstel, G. First-principles calculations for SrTiO₃ (100) surface structure. *Surf. Sci.* **2002**, *513* (1), 211–220.
- (31) Ge, A.; Videla, P. E.; Rudshteyn, B.; Liu, Q.; Batista, V. S.; Lian, T. Dopant-Dependent SFG Response of Rhenium CO₂ Reduction Catalysts Chemisorbed on SrTiO₃ (100) Single Crystals. *J. Phys. Chem. C* **2018**, *122* (25), 13944–13952.
- (32) Fang, F.; Feng, N.; Zhao, P.; Chen, C.; Li, X.; Meng, J.; Liu, G.; Chen, L.; Wan, H.; Guan, G. In situ exsolution of Co/CoO_x core-shell nanoparticles on double perovskite porous nanotubular webs: A synergistically active catalyst for soot efficient oxidation. *Chem. Eng. J.* **2019**, *372*, 752–764.
- (33) Lee, C.; Jeon, Y.; Hata, S.; Park, J.-I.; Akiyoshi, R.; Saito, H.; Teraoka, Y.; Shul, Y.-G.; Einaga, H. Three-dimensional arrangements of perovskite-type oxide nano-fiber webs for effective soot oxidation. *Appl. Catal., B* **2016**, *191*, 157–164.
- (34) Xiong, J.; Wu, Q.; Mei, X.; Liu, J.; Wei, Y.; Zhao, Z.; Wu, D.; Li, J. Fabrication of Spinel-Type Pd_xCo_{3-x}O₄ Binary Active Sites on 3D Ordered Meso-macroporous Ce-Zr-O₂ with Enhanced Activity for Catalytic Soot Oxidation. *ACS Catal.* **2018**, *8* (9), 7915–7930.
- (35) Takata, T.; Domen, K. Defect engineering of photocatalysts by doping of aliovalent metal cations for efficient water splitting. *J. Phys. Chem. C* **2009**, *113* (45), 19386–19388.
- (36) Dhakshinamoorthy, J.; Prasad, A. K.; Dhara, S.; Pullithadathil, B. Anomalous effects of lattice strain and Ti³⁺ interstitials on room-temperature magnetic ordering in defect-engineered nano-TiO₂. *J. Phys. Chem. C* **2018**, *122* (48), 27782–27794.
- (37) Ren, Q.; He, Y.; Wang, H.; Sun, Y.; Dong, F. Photo-switchable oxygen vacancy as the dynamic active site in the photocatalytic NO oxidation reaction. *ACS Catal.* **2022**, *12* (22), 14015–14025.
- (38) Qin, Y.; Xu, R.; Ding, L.; Wang, T.; Guo, D.; Fang, F.; Chang, K. La, Al-dominated stabilization of Cr³⁺ in crystal-remolded SrTiO₃ for efficient visible-light-driven overall water splitting. *J. Catal.* **2024**, *430*, 115317.
- (39) Fang, F.; Zhang, J.; Su, Z.; Xu, F.; Li, J.; Chang, K. Boost of solar water splitting on SrTiO₃ by designing V-ions center for localizing defect charge to suppress deep trap. *J. Catal.* **2023**, *425*, 422–431.
- (40) Tan, H.; Zhao, Z.; Zhu, W.-b.; Coker, E. N.; Li, B.; Zheng, M.; Yu, W.; Fan, H.; Sun, Z. Oxygen vacancy enhanced photocatalytic activity of perovskite SrTiO₃. *ACS Appl. Mater. Interfaces* **2014**, *6* (21), 19184–19190.
- (41) Park, J. S.; Kim, S.; Xie, Z.; Walsh, A. Point defect engineering in thin-film solar cells. *Nat. Rev. Mater.* **2018**, *3* (7), 194–210.
- (42) Qin, X.; Liu, X.; Huang, W.; Bettinelli, M.; Liu, X. Lanthanide-activated phosphors based on 4f-5d optical transitions: theoretical and experimental aspects. *Chem. Rev.* **2017**, *117* (5), 4488–4527.
- (43) Li, X.; Wang, X.; Ding, J.; Ma, M.; Yuan, S.; Yang, Q.; Wang, Z.; Peng, Y.; Sun, C.; Zhou, H.; et al. Engineering active surface oxygen sites of cubic perovskite cobalt oxides toward catalytic oxidation reactions. *ACS Catal.* **2023**, *13* (9), 6338–6350.
- (44) Ji, F.; Men, Y.; Wang, J.; Sun, Y.; Wang, Z.; Zhao, B.; Tao, X.; Xu, G. Promoting diesel soot combustion efficiency by tailoring the shapes and crystal facets of nanoscale Mn₃O₄. *Appl. Catal., B* **2019**, *242*, 227–237.
- (45) Zhao, P.; Feng, N.; Fang, F.; Wan, H.; Guan, G. Surface acid etching for efficient anchoring of potassium on 3DOM La_{0.8}Sr_{0.2}MnO₃ catalyst: An integration strategy for boosting soot and NO_x simultaneous elimination. *J. Hazard. Mater.* **2021**, *409*, 124916.
- (46) Huo, Z.; Chen, Y.; Zhao, P.; Sun, L.; Tan, B.; Ren, L.; Feng, N.; Wan, H.; Guan, G. Promoting the generation of active oxygen species on 3DOM K/LaMnO₃ interface by introducing CeO₂ to boost the NO_x-assisted soot combustion. *Fuel* **2022**, *317*, 123405.
- (47) Chen, Y.; Shen, G.; Lang, Y.; Chen, R.; Jia, L.; Yue, J.; Shen, M.; Du, C.; Shan, B. Promoting soot combustion efficiency by strengthening the adsorption of NO_x on the 3DOM mullite catalyst. *J. Catal.* **2020**, *384*, 96–105.
- (48) Fang, Z.; Wang, H. Densification and grain growth during sintering of nanosized particles. *Int. Mater. Rev.* **2008**, *53* (6), 326–352.
- (49) Liu, J.; Zhao, Z.; Wang, J.; Xu, C.; Duan, A.; Jiang, G.; Yang, Q. The highly active catalysts of nanometric CeO₂-supported cobalt oxides for soot combustion. *Appl. Catal., B* **2008**, *84* (1–2), 185–195.
- (50) Shi, Q.; Liu, T.; Li, Q.; Xin, Y.; Lu, X.; Tang, W.; Zhang, Z.; Gao, P.-X.; Anderson, J. A. Multiple strategies to decrease ignition temperature for soot combustion on ultrathin MnO_{2-x} nanosheet array. *Appl. Catal., B* **2019**, *246*, 312–321.
- (51) Tsai, Y.-C.; Huy, N. N.; Lee, J.; Lin, Y.-F.; Lin, K.-Y. A. Catalytic soot oxidation using hierarchical cobalt oxide microspheres with various nanostructures: Insights into relationships of morphology, property and reactivity. *Chem. Eng. J.* **2020**, *395*, 124939.
- (52) Zhai, G.; Wang, J.; Chen, Z.; An, W.; Men, Y. Boosting soot combustion efficiency of Co₃O₄ nanocrystals via tailoring crystal facets. *Chem. Eng. J.* **2018**, *337*, 488–498.
- (53) Zhao, Z.; Zheng, D.; Guo, M.; Yu, J.; Zhang, S.; Zhang, Z.; Chen, Y. Engineering olefin-linked covalent organic frameworks for photoenzymatic reduction of CO₂. *Angew. Chem., Int. Ed.* **2022**, *61* (12), No. e202200261.
- (54) Odoh, S. O.; Schreckenbach, G. DFT Study of uranyl peroxy complexes with H₂O, F⁻, OH⁻, CO₃²⁻, and NO₃⁻. *Inorg. Chem.* **2013**, *52* (9), 5590–5602.
- (55) Mao, C.; Cheng, H.; Tian, H.; Li, H.; Xiao, W.-J.; Xu, H.; Zhao, J.; Zhang, L. Visible light driven selective oxidation of amines to imines with BiOCl: Does oxygen vacancy concentration matter? *Appl. Catal., B* **2018**, *228*, 87–96.
- (56) Wu, X.; Lin, F.; Xu, H.; Weng, D. Effects of adsorbed and gaseous NO_x species on catalytic oxidation of diesel soot with MnO_x-CeO₂ mixed oxides. *Appl. Catal., B* **2010**, *96* (1–2), 101–109.
- (57) Zhao, M.; Deng, J.; Liu, J.; Li, Y.; Liu, J.; Duan, Z.; Xiong, J.; Zhao, Z.; Wei, Y.; Song, W.; et al. Roles of surface-active oxygen species on 3DOM cobalt-based spinel catalysts M_xCo_{3-x}O₄ (M= Zn and Ni) for NO_x-assisted soot oxidation. *ACS Catal.* **2019**, *9* (8), 7548–7567.
- (58) Ou, Y.; Wang, B.; Xu, N.; Song, Q.; Liu, T.; Xu, H.; Wang, F.; Li, S.; Wang, Y. Tandem Electric-Fields Prolong Energetic Hot Electrons Lifetime for Ultra-Fast and Stable NO₂ Detection. *Adv. Mater.* **2024**, *36* (30), 2403215.
- (59) Urán, L.; Gallego, J.; Ruiz, W.; Bailón-García, E.; Bueno-López, A.; Santamaría, A. Monitoring intermediate species formation by DRIFT during the simultaneous removal of soot and NO_x over LaAgMnO₃ catalyst. *Appl. Catal., A* **2019**, *588*, 117280.

NOTE ADDED AFTER ASAP PUBLICATION

This paper was originally published ASAP on December 26, 2024. The Supporting Information file was updated, and the paper reposted on December 27, 2024.